SPACE TELESCOPE SCIENCE INSTITUTE
Operated for NASA by AURA

Instrument Science Report WFC3 2009-31

WFC3 SMOV Proposal 11450: The Photometric Performance and Calibration of WFC3/UVIS

J. S. Kalirai, J. MacKenty, A. Rajan
S. Baggett, R. Bohlin, T. Brown, S. Deustua, R. A. Kimble, A. Riess, E. Sabbi, and the WFC3 Team

November 18, 2009

Abstract

We present the photometric calibration of the UVIS camera on WFC3. Following successful installation during Servicing Mission 4, we began a primary calibration program to measure the photometric zero points of 37 high priority filters on the UVIS1 CCD. Additional secondary observations obtained as a part of the UVIS Contamination Monitor Program with both UVIS1 and UVIS2 are also analyzed (CAL11426 – Baggett et al. 2009). All measurements are made from a set of high signal-to-noise imaging observations of the white dwarf standards GD 153 (primary program) and GRW+70d5824 (secondary program). We find that the total system throughput of both CCDs is significantly better than expected from the Thermal Vacuum 3 (TV3) testing campaign, with efficiency gains of ∼10% at the blue and red ends of the spectral coverage, and ∼20% near the central wavelength, 5500 Å. Repeat visits in a subset of filters separated by approximately 1 day, 1 week, and 1 month indicate photometric stability in the measured counts to better than 0.5%. We update the Exposure Time Calculator (ETC) with these preliminary results by fitting a smooth curve (2nd order polynomial) to the ratios of the efficiency gains over previous predictions, in the medium and wide band filters. This polynomial is interpolated at a fine wavelength grid and multiplied into the SYNPHOT throughput routines. We also provide photometric zero points for the UVIS camera in three photometric systems, STMAG, ABMAG, and VEGAMAG. A much more detailed Cycle 17 calibration plan, including observations targeting multiple primary standards, and with all filters on both CCDs, begins in October 2009.

1. The New WFC3 Camera on HST

Immediately after its successful installation on the Hubble Space Telescope (HST) in May 2009, the Wide Field Camera 3 (WFC3) became the workhorse instrument on what has become scientifically the most productive observatory in/around the world. The instrument contains two cameras that provide high-resolution imaging over a wavelength range extending from the UV, through the optical, to the NIR. The UVIS channel specifically extends from the blue cutoff at ∼2000 Å to ∼9500 Å, and contains a total of 62 narrow, medium, and wide band filters, and one grism. The camera consists of two CCDs subtending a total angular field of view of 162 × 162 arcseconds, with a pixel scale of 0.04 arcseconds.

In this document, we present the first analysis of photometric imaging observations obtained with WFC3/UVIS during the three month period following the camera's installation on HST. Two separate programs designed for the Servicing Mission Orbital Verification 4 (SMOV4) Phase are analyzed, CAL11450 (Kalirai & Brown) and CAL11426 (Baggett et al.). Each of these programs targets a bright spectrophotometric standard star with the goal of measuring the photometric performance and stability of the camera. A calibration of the WFC3 IR channel is presented in Kalirai et al. (2009a).

Below, we first summarize the characterization of the performance of the camera based on several ground testing campaigns prior to launch, and then describe the first on-orbit observations of calibrated white dwarf stars from programs CAL11450 and CAL11426. Next, we briefly describe the techniques adopted to process the raw HST data including removal of cosmic rays. Aperture photometry is performed on the flux standards in these final images. The resulting measurements are compared to the predictions from the present WFC3 Exposure Time Calculator (ETC). These comparisons conclusively show that an overall sensitivity boost to the ETC is required, and we outline the method used to implement this change for current and future users. From here on, we refer to these predictions as counts measured in the STSDAS package SYNPHOT, which is the engine behind the ETC.

Finally, we place these results into an overall scientific context by discussing the impact of these findings as they pertain to general astronomical observations with HST. In terms of spectral coverage, imaging depth, and resolution, WFC3 will be the preferred HST instrument for accomplishing many of the scientific goals that are at the forefront of astronomical research today.

2. Ground Testing of the WFC3 UVIS Detector

The system throughput of the UVIS camera on WFC3 was measured in three extensive Thermal Vacuum (TV) campaigns. These tests were carried out at NASA/GSFC using an optical stimulus called "CASTLE". The "CASTLE" system illuminates the focal plane of the detector with a high signal, flux-calibrated monochromatic light source, therefore allowing the resulting throughput to

be measured with standard aperture photometry. Given changes in the calibration of the optical stimulus, adjustments to the sensitivity of the photomultiplier tubes, and even the use of different UVIS detectors in the camera, the three different TV tests yielded significant throughput variations (see Brown & Reid 2005; Brown 2007; Brown 2008).

The current characterization of the overall system throughput, built into SYNPHOT, results from the final "CASTLE" aperture photometry measurements in TV3 (Spring 2008 – Brown 2008). The full model that yields the expected SYNPHOT counts for a given observational setup includes a contribution from the following components: the HST Optical Telescope Assembly (OTA), pick-off mirror, mirror reflectivity, filter throughput, outer window, inner window, and the quantum efficiency (QE) of the detector. The throughputs for each of these components were compiled from a number of sources including the Goddard Space Flight Center, Detector Characterization Laboratory (DCL), and Ball Aerospace (T. Brown, private communication). The new results from the final TV3 analysis, which reflected a downward revision in the measured counts versus expected counts from earlier campaigns, were folded into the QE (i.e., the initial measurements from the DCL were updated).

3. First On-Orbit Observations

The primary objective of the present SMOV4 calibration is to provide the first on-orbit estimate of the throughput of the UVIS camera on WFC3 in a set of high priority filters. Our specific goal is to characterize the photometric zero points to an accuracy of a few percent in the medium and wide band filters. A secondary goal is to monitor this throughput for temporal variations. We designed an observational program to target a single bright HST spectrophotometric standard star in 37 essential UVIS filters, summarized in Table 1 (16 highest priority, 20 lower priority, and 1 ERO filter, chosen based on Cycle 17 usage statistics).[1] A comparison of the measured counts from high signal-to-noise (S/N) observations of this standard star with its well understood absolute flux calibration (see below) will yield the true on-orbit throughput of the instrument.

The three primary HST spectrophotometric standards used by previous/current instruments are the hot DA (hydrogen atmosphere) white dwarfs G191-B2B ($V = 11.77$), GD 153 ($V = 13.35$), and GD 71 ($V = 13.03$). The spectrum of these stars over our wavelength range exhibit only pressure broadened Balmer lines. Each of these stars has been observed with STIS, ACS, WFPC2, and NICMOS, and the resulting data has been analyzed and discussed in several papers, Bohlin, Colina, & Finley (1995); Bohlin (1996); Bohlin (2000); Bohlin, Dickinson, & Calzetti (2001); Bohlin (2007). The Balmer absorption lines of these stars, as measured from the ground, have been modeled to yield the fundamental properties of each of the three white dwarfs (e.g., temperature and surface gravity – see e.g., Bergeron, Saffer, & Liebert 1992), thereby allowing the construction

[1]SMOV4 proposal CAL11450 – J. Kalirai & T. Brown; see Kalirai et al. 2009b.

Table 1: WFC3/UVIS Filters Exposed in SMOV4

Filter	Pivot λ (Å)	Width λ (Å)[a]	Filter	Pivot λ (Å)	Width λ (Å)[a]
F218W	2228.5	351.7	F502N	5009.6	57.8
F225W	2372.7	547.3	F547M	5447.4	714.0
F275W	2710.1	480.8	F555W	5308.1	1595.1
F280N	2833.5	22.9	F600LP	7450.5	(4000)
F300X	2822.5	753.0	F606W	5887.4	2304.2
F336W	3354.8	553.8	F621M	6218.6	631.0
F343N	3435.2	140.0	F625W	6241.3	1575.4
F350LP	5857.3	(4500)	F645N	6453.6	85.0
F373N	3730.2	39.2	F656N	6561.4	13.9
F390M	3897.3	210.5	F658N	6584.0	23.6
F390W	3924.4	953.0	F665N	6655.9	109.0
F395N	3955.2	72.9	F673N	6765.9	100.5
F410M	4109.0	182.8	F689M	6876.3	708.6
F438W	4326.5	676.8	F763M	7613.5	798.6
F467M	4682.6	218.0	F775W	7648.5	1486.0
F469N	4688.1	37.2	F814W	8029.5	2543.3
F475W	4773.7	1488.9	F845M	8437.5	886.7
F475X	4941.4	2199.6	F953N	9530.5	84.6
F487N	4871.4	48.4			

[a]See WFC3 Instrument Handbook (IHB) for more details.

of a model out to very short and long wavelengths (Finley, Koester, & Basri 1997; Bohlin 2000). These models agree with the STIS spectra to better than 1%, indicating a superb absolute flux calibration. Therefore, the predicted counts from convolving our instrument throughput with the model spectrum of either of these three stars yields a very accurate calibration. Other HST white dwarf standards also exist, but their measured fluxes are less accurate.

Given the SMOV4 timing windows, we observed GD 153 as our primary calibration source. The detailed observations consisted of an initial visit exposing the standard star in all 37 filters, with repeat visits at 1 day, 7 days, and 31 days in a set of 8 wide band filters. The exposures were short (e.g., few seconds) and set to ensure a high S/N of $\gtrsim$100 in each of the individual observations, avoiding saturation. All observations were conducted on the UVIS1 CCD of WFC3, with a 512 $\times$ 512 subarray on Amp A (UVIS1-C512A-SUB), and over a four point (non-integer) dither pattern extending $\sim$40 pixels. A log of these observations is provided in Table 2.

In addition to these primary observations, we also leverage the data obtained in the UVIS Contamination Monitor Program (CAL11426 – Baggett et al. 2009). These observations target another bright white dwarf standard, GRW+70d5824 (V = 12.77), in a set of 14 blue filters ($\lambda <$ 5000 Å) including additional observations in the commonly used F606W and F814W filters. The observations are taken with the 512 $\times$ 512 subarray with a two-point dither pattern. Both of the WFC3 CCDs were exposed on Amp A and Amp C and all observations were repeated once per week.

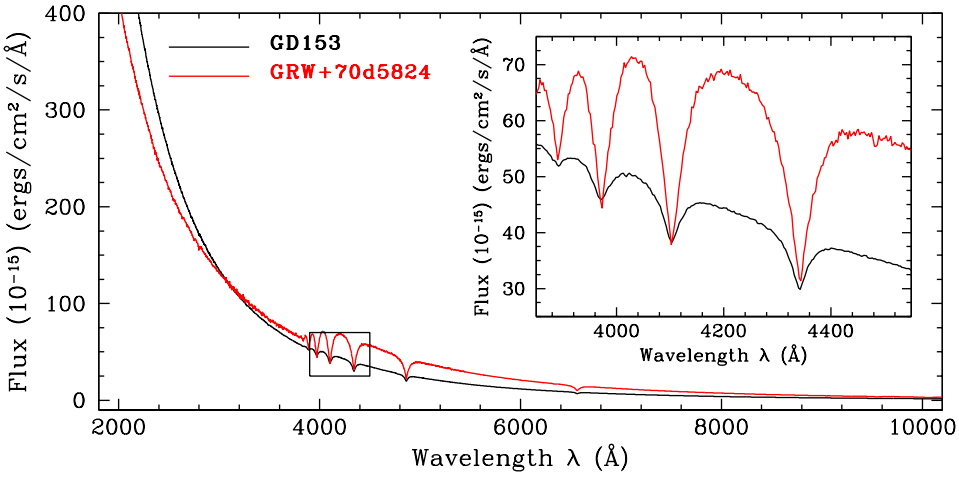

Fig. 1.— *The HST/STIS spectra of both GD 153 (black) and GRW+70d5824 (red). Both white dwarfs show a smooth continuum with hydrogen Balmer lines (DA stars). We zoom into several of these lines in the inset panel. The absolute flux of GD 153 is known to <1% based on the comparison of a pure hydrogen model with the STIS spectrum of the star. The model has* $T_{\rm eff}$ *= 38,700 K and log(g) = 7.66 (Finley, Koester, & Basri 1997), derived from fits to ground based spectra of the Balmer lines. The absolute flux calibration of GRW+70d5824 is not as well understood as GD 153.*

There is only one HST STIS observation, and a model spectrum has not been critically compared to the data. Therefore, the absolute flux of GRW+70d5824 is less precise than for GD 153. We analyze these observations of GRW+70d5824 to show that the UVIS2 response is similar to that of UVIS1. The initial observations of this star were taken before the focus adjustment of WFC3 was finalized, and some of the images of the star were executed on a bad column, and are therefore ignored here. We summarize the three sets of observations that we utilize for this star in Table 2 (see Baggett et al. 2009 for more information). The STIS spectra of both stars appear in Figure 1, taken from the STScI CALSPEC webpage.[2]

4. Data Processing and Aperture Photometry

The raw images were retrieved from the Multimission Archive at Space Telescope (MAST) and processed with the IRAF/STSDAS pipeline program calwf3. The steps performed included a bias, dark, and flat field correction to the raw data, yielding the processed _flt images on which we perform photometry. These observations represented some of the first UVIS external exposures with WFC3, and therefore the data were reprocessed several times to reflect updated bias files as

[2]`http://www.stsci.edu/hst/observatory/cdbs/calspec.html`, see Bohlin, Dickinson, & Calzetti (2001) and references therein for more information.

Table 2: WFC3/UVIS SMOV4 Photometric Calibration Observations

Target	Filters (Exp Time [s])	CCD	Orbits
Visit 11 – 2009-07-13			
GD 153	F218W (2), F225W (1), F275W (1), F280N (10), F300X (1) F336W (1), F343N (1), F373N (10), F350LP (0.5), F390M (2) F390W (1), F395N (10), F410M (2), F438W (1), F467M (2) F469N (10), F475W (1), F475X (1), F487N (10), F502N (10) F547M (1), F555W (1), F600LP (1), F606W (1), F621M (2) F625W (1), F645N (10), F656N (40), F658N (20), F665N (20) F673N (10), F689M (2), F763M (2), F775W (2), F814W (2) F845M (10), F953N (60)	UVIS1	5
Visit 12 – 2009-07-14			
GD 153	F225W (1), F275W (1), F336W (1), F390W (1) F438W (1), F555W (1), F606W (1), F814W (2)	UVIS1	1
Visit 13 – 2009-07-21			
GD 153	F225W (1), F275W (1), F336W (1), F390W (1) F438W (1), F555W (1), F606W (1), F814W (2)	UVIS1	1
Visit 14 – 2009-08-11			
GD 153	F225W (1), F275W (1), F336W (1), F390W (1) F438W (1), F555W (1), F606W (1), F814W (2)	UVIS1	1
Visit 31 – 2009-07-15			
GRW+70d5824	F218W (3.9), F225W (1.4), F275W (1.3), F280N (23.8) F300X (0.5), F336W (0.8), F343N (1.6), F373N (10.2) F395N (5.3), F390M (2.1), F390W (0.5), F410M (2.0) F438W (0.5), F467M (1.8), F606W (0.5), F814W (1.0)	UVIS1/UVIS2	1
Visit 41 – 2009-07-22			
GRW+70d5824	F218W (3.9), F225W (1.4), F275W (1.3), F280N (23.8) F300X (0.5), F336W (0.8), F343N (1.6), F373N (10.2) F395N (5.3), F390M (2.1), F390W (0.5), F410M (2.0) F438W (0.5), F467M (1.8), F606W (0.5), F814W (1.0)	UVIS1/UVIS2	1
Visit 51 – 2009-07-29			
GRW+70d5824	F218W (3.9), F225W (1.4), F275W (1.3), F280N (23.8) F300X (0.5), F336W (0.8), F343N (1.6), F373N (10.2) F395N (5.3), F390M (2.1), F390W (0.5), F410M (2.0) F438W (0.5), F467M (1.8), F606W (0.5), F814W (1.0)	UVIS1/UVIS2	1

more on-orbit data became available. An important consideration is that all measurements that follow have been made using processed data with ground flats; and, therefore, both low order and pixel-to-pixel corrections will be improved over time. Detailed information on each of the data reduction steps within calwf3 is presented in the WFC3 Data Handbook, `http://www.stsci.edu/hst/wfc3/documents/handbooks/currentDHB/WFC3_longdhbcover`.

We performed two independent analysis of the processed _flt images. The first set utilized single image cosmic ray rejection with the Laplacian edge detection scheme, lacos, discussed in van Dokkum (2001)[3], followed by photometry with the standalone version of DAOPHOT (Stetson 1987; 1994). After some tweaking of the input parameters to reflect WFC3 characteristics, the lacos program efficiently removed virtually all cosmic rays while leaving the flux of the source star unsubtracted in all cases. In the second analysis, we removed cosmic rays by flagging hits that appeared only on one of our multiple dithered exposures after registering the frames. Photometry was also performed on these images using the analogous DAOPHOT program built into IRAF.

The two independent analysis discussed above are in excellent agreement with one another. As an example, for an aperture with $R = 0.4$ arcseconds, 97% of the hundreds of individual measurements of GD 153 agree to within 0.2%, the approximate level of the uncertainties in the count statistics. The lacos program therefore presents a powerful technique to clean cosmic rays on single WFC3 images. As some WFC3 programs will not have the benefit of dithered or CR-SPLIT observations, we present a brief discussion of our choice of parameters and illustrate some results of input vs output images in a separate ISR (Kalirai 2009c). For the remaining discussion to follow, our nominal photometric performance reflects the results from the second set of analyses, using dithered observations to remove cosmic rays.

We performed aperture photometry on all individual cosmic ray cleaned images in a set of 13 apertures with radii of 0.10 to 3.00 arcseconds (2.5 to 75 pixels). The specific apertures chosen reflect all twelve of the aperture options available in the current WFC3 ETC, including one larger radius at 3.00 arcseconds (i.e., 0.10, 0.15, 0.20, 0.25, 0.30, 0.40, 0.50, 0.60, 0.80, 1.00, 1.50, 2.00, and 3.00 arcseconds). The sky was calculated as the modal value in an annulus extending from 3.0 to 5.0 arcseconds. The modal sky value was chosen over other statistical measures (such as the mean or median) as it better reflects the sky in a typical pixel and will not be skewed by tails in the overall distribution. We experimented with other statistical measures of the sky and found negligible differences that were a fraction of a percent in all but the largest annuli (still <1%). The cause of the small variations at these large radii are partly related to our use of a preliminary flat field correction which will improve over time, and also to the fact that the number of pixels in our sky annulus is only a few times larger than our largest science aperture (and therefore the statistics in the sky subtraction are limited).

[3]The lacos program is available at `http://www.astro.caltech.edu/~pgd/lacosmic/`.

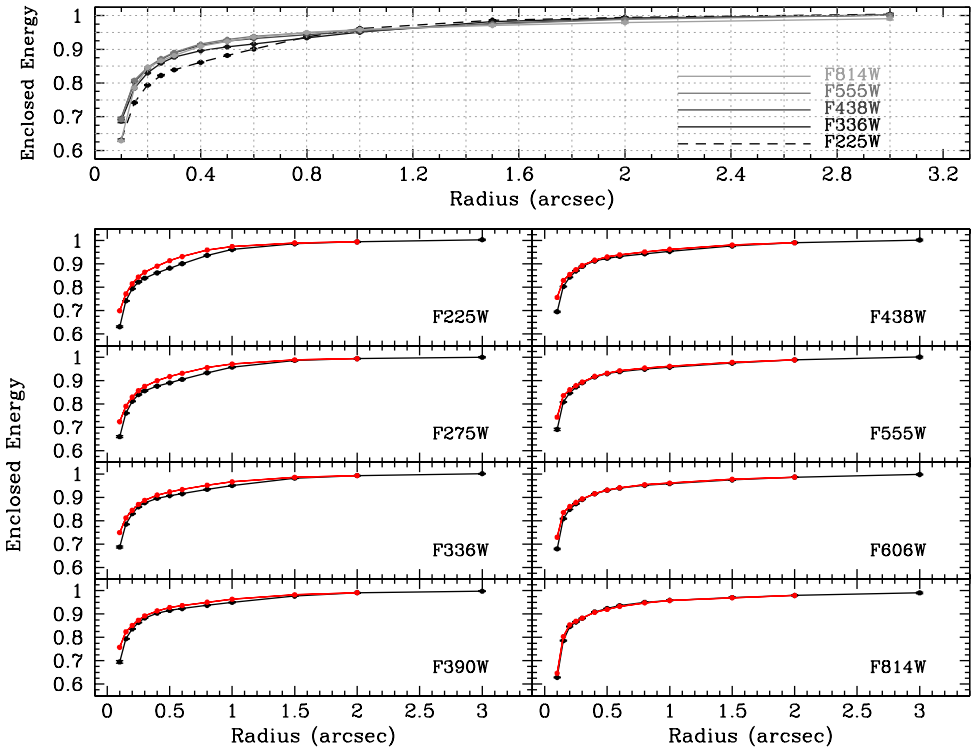

Fig. 2.— *Top – The total energy enclosed in a set of five broadband filters as a function of aperture size for the UVIS1 observations of GD 153. Each of the curves has been normalized to the expected counts at 2 arcseconds relative to an infinite aperture, based on the preflight enclosed energy curves (the counts at 2 arcseconds are within 2% of the total counts at all wavelengths). Bottom – A closer look at the comparison of our on-orbit measured enclosed energy curves (black) to the pre-flight model (red). At ultraviolet wavelengths, the model curves over predict the measured counts at intermediate radii by up to 3 – 4%, as discussed in the text.*

5. Enclosed Energy Curves and On-Orbit Aperture Corrections

We illustrate the measured counts in five broadband filters, over all apertures, spanning almost the full UVIS wavelength range in Figure 2 (top). The data consists of averaged fluxes from all individual exposures of the primary spectrophotometric standard GD 153. This includes the four dither positions on each visit, and all four visits in the program. The errors in the means are also plotted, although these are typically smaller than the point sizes on this scale. The total counts are normalized in each filter to the estimated enclosed flux at the 2 arcsecond radius aperture, based on a pre-flight model (see below). At all wavelengths, the model predicts that the measured flux at 2 arcseconds is within 2% of the total flux (i.e., that measured for an aperture with infinite radius). The general shape of these empirically calculated enclosed energy diagrams is very similar at most wavelengths, with the only significant exceptions being the ultraviolet measurements, where the curves rise more slowly.

A closer comparison of these data provide a preliminary estimate of the accuracy of the preflight enclosed energy calculations. In Figure 2 (bottom), we illustrate both the model curves (e.g., those that are presently being used to interpolate the total measured counts to a specific aperture) vs our new empirically calculated curves. The model curves (red) over predict the counts at radii of $\sim$0.2 – 1.5 arcseconds at the bluest wavelengths. In the most extreme case, F225W, the model is over predicting the enclosed energy by 3 – 4% at 0.5 arcseconds. The discrepancy becomes less severe for redder wavelengths, and the two curves overlap nicely at $\lambda \gtrsim 4500$ Å. The cause of the mismatch at ultraviolet wavelengths is likely related to the spatial frequency limitations of the Optical Telescope Assembly mirror wavefront error maps, and is discussed further in the SMOV4 UVIS PSF Wing Evaluation Program (CAL11438 – Hartig & Dressel 2009). Indeed, the images of our bright spectrophotometric standards in ultraviolet filters such as F225W show a faint "halo" surrounding the star, indicating that a small fraction of the central flux has been scattered to larger radii.

Although the ETC can predict the counts in a given filter for an aperture with a specific radius, we have accounted for the above scattered light concerns by recalculating all SYNPHOT total flux measurements to a specific aperture based on these on-orbit enclosed energy curves. The broad band data shown in Figure 2 defines the table of corrections, and narrow/medium band filters not shown here are interpolated within that grid. We present these enclosed energy fractions, derived solely from our GD 153 observations, in Table 3. Although expected to be very similar, the actual aperture corrections that will be reflected in the upcoming SYNPHOT update will also utilize very high S/N observations of this star in the wings of the PSF (Hartig & Dressel 2009).

Table 3: Preliminary WFC3/UVIS On-Orbit Enclosed Energy Fractions

Radius (")	F225W	F275W	F336W	F390W	F438W	F555W	F606W	F814W
λ (Å)	**2341**	**2715**	**3361**	**3905**	**4319**	**5310**	**5907**	**8305**
0.10	0.631	0.660	0.687	0.695	0.695	0.691	0.679	0.628
0.15	0.742	0.761	0.785	0.794	0.803	0.808	0.808	0.786
0.20	0.794	0.812	0.830	0.836	0.843	0.847	0.848	0.846
0.25	0.822	0.840	0.859	0.864	0.870	0.872	0.872	0.866
0.30	0.839	0.856	0.877	0.883	0.889	0.891	0.891	0.882
0.40	0.862	0.876	0.896	0.904	0.912	0.915	0.915	0.909
0.50	0.882	0.890	0.907	0.915	0.924	0.930	0.930	0.924
0.60	0.901	0.905	0.916	0.923	0.932	0.938	0.939	0.936
0.80	0.937	0.933	0.934	0.937	0.943	0.949	0.951	0.950
1.00	0.962	0.958	0.951	0.950	0.953	0.957	0.958	0.959
1.50	0.986	0.986	0.982	0.977	0.977	0.975	0.974	0.971
2.00	0.995	0.994	0.993	0.991	0.991	0.989	0.986	0.979

6. Photometric Stability – Spatial and Temporal

The SMOV4 observations of GD 153 are obtained using a four point dither pattern on the 512 × 512 subarray on Amp A (UVIS1-C512A-SUB, near one of the four corners of the camera). These data therefore can not be used to put strong constraints on the photometric stability as a function of spatial position on the detector. Nevertheless, we illustrate the comparison of photometry measured at these four dither positions (separated by $\lesssim$40 pixels), for all 37 filters, in Figure 3. The observations shown in this comparison were all obtained over a continues 5 orbit sequence in Visit 11 of our program. The measured standard deviations, across all filters, in apertures with radii 0.2, 0.4, and 0.8 arcseconds are <1% and at the largest aperture of $R = 2.0$ arcseconds is 1.1%. The increased scatter in the larger aperture results from several factors. First, the number of pixels in our sky annulus, from 3.0 – 5.0 arcseconds, is only 4 times higher than the number in the science aperture, and thus the statistical subtraction of the sky value is more uncertain than for smaller apertures. Second, as mentioned earlier, the calibrated _flt images that we are using have been constructed with a ground-based pixel-to-pixel flat field correction and no low-frequency flat field correction. For larger apertures on the detector, small scale variations in these calibrations (e.g., ground vs on-orbit) can produce measurable differences in the counts. Finally, these analysis predated the construction of the final geometric distortion solution of the UVIS camera, and therefore a differential pixel area map correction was not applied to the _flt images (note, a fixed correction was applied to the entire counts – see below). The actual area of WFC3 pixels on this subarray vary by about 0.1% going across the diameter of our sky annulus.

Overall, the measured dispersion in our apertures is not much larger than expected given the photometric errors (error bars). Strictly from Poisson noise, we expect the uncertainty in the counts to be <0.5% for all of our wide band observations, and 0.5 – 1.0% for several of the narrow and medium bands (in *single* exposures). These observations therefore demonstrate that, over this small region of the detector, the photometry is stable to <1%. A more detailed discussion of the overall photometric stability over the entire detector, from an analysis of dithered globular cluster observations with many stars, is provided in the UVIS Flat Field Uniformity Program (CAL11452 – Sabbi et al. 2009).

The temporal stability of WFC3 can be characterized from the three sets of repeat observations. At time intervals of 1 day, 1 week, and 1 month, we re-observed GD 153 in the same set up as described above in eight broadband filters; F225W, F275W, F336W, F390W, F438W, F555W, F606W, and F814W. We illustrate the photometric scatter from these observations in Figure 4. The grey data points illustrate the ratio of the measured counts in each of the 16 sets of observations to the overall mean (e.g., four dither positions at four epochs), whereas the darker points illustrate the comparison of the averaged counts from each of the four epochs to the mean, with errors in the mean. For the latter, we measure the standard deviation across all filters to be <0.5%, indicating temporal stability at the level of the individual uncertainties.

As a secondary check on the temporal stability, we also consider the observations from the

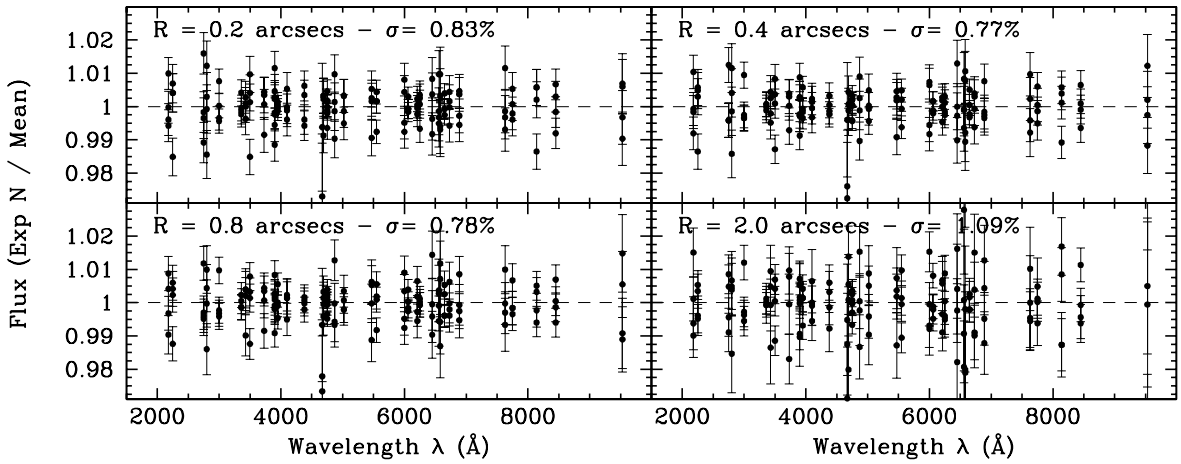

Fig. 3.— *The comparison of photometry for GD 153 measured at four dither positions separated by* $\lesssim$*40 pixels, during a single visit. All 37 filters are shown, for apertures of 0.2, 0.4, 0.8, and 2.0 arcseconds. The standard deviation of all points is indicated in the separate panels, and illustrates photometric stability over this small area of the detector to* $\lesssim$*1%, comparable to the photometric errors. The images processed for these measurements do not utilize full on-orbit calibration frames (such as flat fields) and have not been corrected for relative variations in the area of the pixels from the distortion solution. Therefore, the scatter in these data should be taken as an upper limit to what will eventually be measured for WFC3 over a similar area.*

UVIS Contamination Monitor Program (CAL11426 – Baggett et al. 2009), in which the bright white dwarf standard GRW+70d5824 was observed in 16 filters at two dither positions, on both UVIS CCDs. The results from that program demonstrate that the photometry is stable to within 2% as a function of wavelength and time.

7. Absolute WFC3/UVIS Throughput

The present data set represents the first on-orbit measurements of the throughput of WFC3/UVIS, and is aimed at correcting the calibration that comes from ground tests during TV3. This calibration is essential to understand the sensitivity of the instrument and to allow users to predict the expected counts in a given observation with WFC3/UVIS. The throughputs measured during TV3 were folded into the WFC3 component tables that are accessed by the STSDAS package SYNPHOT. The present sensitivity corrections are by no means the final calibration of the instrument, however we expect future observations to represent a fine-tuning of the throughput presented here.

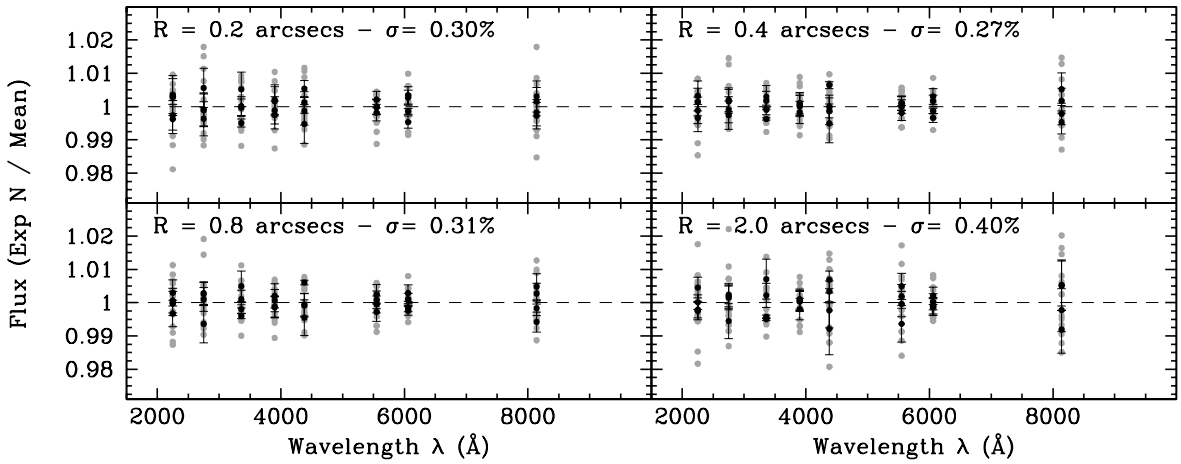

Fig. 4.— *The temporal stability of the detector is measured by comparing the photometry of GD 153 in eight wide band filters measured at four epochs, the initial observations, after 1 day, after 1 week, and after 1 month. The grey data points indicate all individual measurements at four dither positions in each of the four visits, and the darker points illustrate the comparison of the averaged counts from each of the four visits. The standard deviation across all eight filters in the latter is <0.5% for all apertures, indicating temporal stability at the level of the individual photometric uncertainties.*

7.1 Comparing On-Orbit Measurements to Ground Tests

Having demonstrated both spatial and temporal stability of the instrument, we derive the final count rate of GD 153 in all 37 filters by averaging the individual photometry measurements at each of the four dither positions, and at each of the four epochs for the eight broadband filters. The default aperture for the photometry is taken be $R = 0.4$ arcseconds. Next, we use the SYNPHOT package to predict the count rate of GD 153 in each of these 37 filters, and scale these to 0.4 arcseconds based on our measured on-orbit enclosed energy fractions in Table 3. This calculation is based on convolving the total instrument response, as calibrated using the TV3 data, with a model fit of the observed spectrum of the white dwarf standard (Bohlin 2000; Bohlin, Dickinson, & Calzetti 2001). Before comparing these to one another, we correct the observed counts for a global offset that reflects the difference in area of the pixels on WFC3 at the position of our subarray to the center of the field. Based on the pixel area map, the pixels at the location of the UVIS1-C512A-SUB subarray are 3% smaller than those at the center of the detector. As the _flt images have been flat fielded, but not corrected for geometric distortion, the smaller pixels have counts that are boosted relative to larger pixels, and so we multiply all of our measured counts by 0.97 to remove this factor. With this correction, the resulting throughput comparisons are equivalent to those that

would be measured both at the center of the _flt images and on future _drz (e.g., drizzled) images.[4] We present an expanded discussion of the WFC3 pixel area maps in Kalirai et al. (2009d), including the rationale behind the normalization of the maps and the (positive) impact for users wishing to compare photometry on _flt and _drz images.

The comparison of our on-orbit measurements to the SYNPHOT estimates, based on ground calibration, is shown in Figure 5. Over the entire wavelength range of WFC3/UVIS, the on-orbit measurements show a higher throughput than the TV3 calibration. At the blue and red ends of the spectral coverage, the detector is 5 – 10% more sensitive and this rises to 15 – 20% at central wavelengths (e.g., $\lambda \sim$5000 Å). We have separated the medium and wide band filters (darker filled circles) from the narrow, x-wide, and long pass filters (grey crosses) in this Figure to illustrate that the latter have much more scatter. This is not surprising considering these filters are susceptible to fringing effects at longer wavelengths, stellar absorption features in the calibration spectrum (e.g., the Hα in GD 153), and generally have lower S/N observations than the wide band observations. Additionally, the uncertainties in the bandpass shape and the wavelengths of the bandpass edges represent a larger fraction of the integrated area under the throughput curve for these filters, leading to larger overall uncertainties. Although these filters generally agree with the trend traced by the medium and wide band filters, we ignore them in the subsequent calibration given the larger scatter.

The one extreme data point that merits a brief discussion on this plot is the F336W filter at $\lambda = 3355$ Å. The counts measured in this filter are systematically $\sim$5% higher than expected from the general trend. This filter is known to suffer from bowtie (QEH) effects in the ground flat field (Sabbi et al. 2008). The bowtie effects are especially strongest near the corners of the detector, exactly where the subarray is located. Further, the magnitude of the effect is similar to the apparent gain in efficiency. Given these concerns, we have excluded this single wide band filter from the analysis that follows.

The source of the general mismatch between the TV3 calibration and our on-orbit measurements is not known. A possible explanation may be related to the accuracy of the "CASTLE" apparatus. As we mentioned above, the actual TV3 calibration resulted in a downward revision of the detector QE, as compared to earlier tests (Brown 2008). The magnitude of this revision was 5 – 10%, being highest at about 6000 Å, close to the wavelength where our on-orbit measurements indicate the largest discrepancy. Interestingly, a similar result was also seen in the first on-orbit observations with the Advanced Camera for Surveys (ACS). As Sirianni et al. (2002) show, their observed counts were 2 – 22% higher than the predicted SYNPHOT counts from ground calibration. As the calibration systems for the two instruments were not related, this points to a calibration error in a common (on-orbit) component (e.g., the HST Optical Telescope Assembly). In any case, some fraction of the gain that we are seeing over the ground tests surely reflects the true detector QE, however it is unclear whether all of it should be attributed to that component. One of the

[4]The IDCTAB and geometric distortion solution were unavailable at the time of this analysis, see Khozurina-Platais et al. (2009).

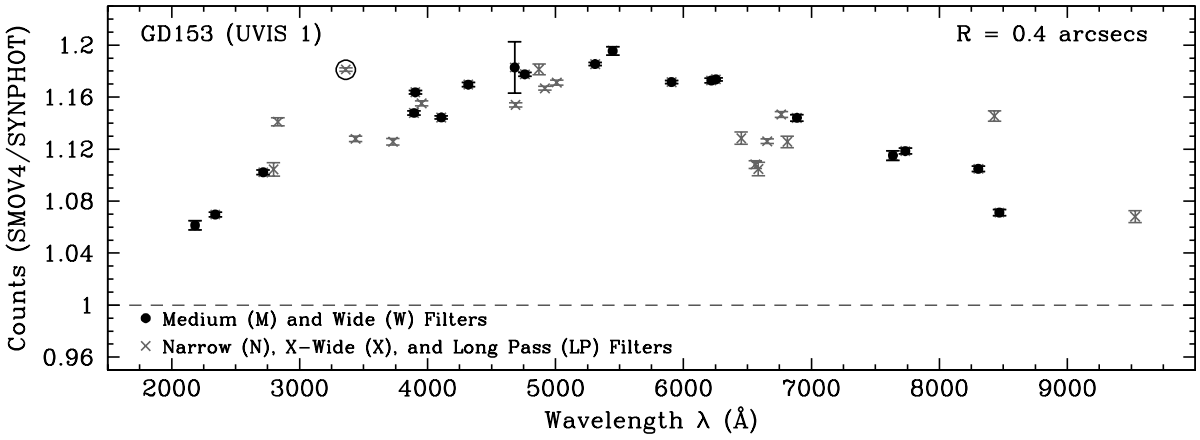

Fig. 5.— *The absolute comparison of our measured photometry for GD 153 to SYNPHOT predictions that were calibrated based on TV3 ground tests. The photometry for multiple dither positions and epochs has been averaged together, with error bars representing the error in the mean measurements. The darker filled circles illustrate the medium and wide band filters and the grey crosses display the narrow, x-wide, and long-pass filters. The one encircled cross is the F336W filter, as discussed in the text. Over the entire wavelength range of WFC3/UVIS, the on-orbit measurements show a higher throughput than the TV3 calibration. At wavelengths in the middle of our spectral coverage, 4000 – 7000* Å*, the gain in efficiency is 15 – 20%, dropping to 5 – 10% at blue and red wavelengths.*

several other component tables may need a revision. This clearly warrants a closer investigation in the future; for now, we factor a new correction term (i.e., fudge factor) based on the total throughput ratio of the on-orbit measurements vs TV3 predictions. For the purpose of SYNPHOT count predictions from a given instrumental setup, this new correction term is simply an additional component that is multiplied into the previous chain of tables.

7.2 Implementing the On-Orbit Correction

In Figure 5 we have plotted the ratio of measured to predicted counts at discrete wavelengths corresponding to the pivot wavelength of the given filter. In reality, each of these bandpasses has a width and covers a broad wavelength range, overlapping neighboring filters in spectral coverage. Therefore we choose not to apply a fixed correction at the pivot wavelength of each filter, which would result in a choppy (with respect to wavelength) correction factor (e.g., see De Marchi 2004). Rather, we adopt an iterative technique that compares synthetic photometry, as calculated after folding in our new smooth correction to SYNPHOT, to the measured counts. The advantage of this approach is that SYNPHOT will take the integral of the actual bandpass with the full throughput, including the correction factor, and will yield output photometry that then determines a new

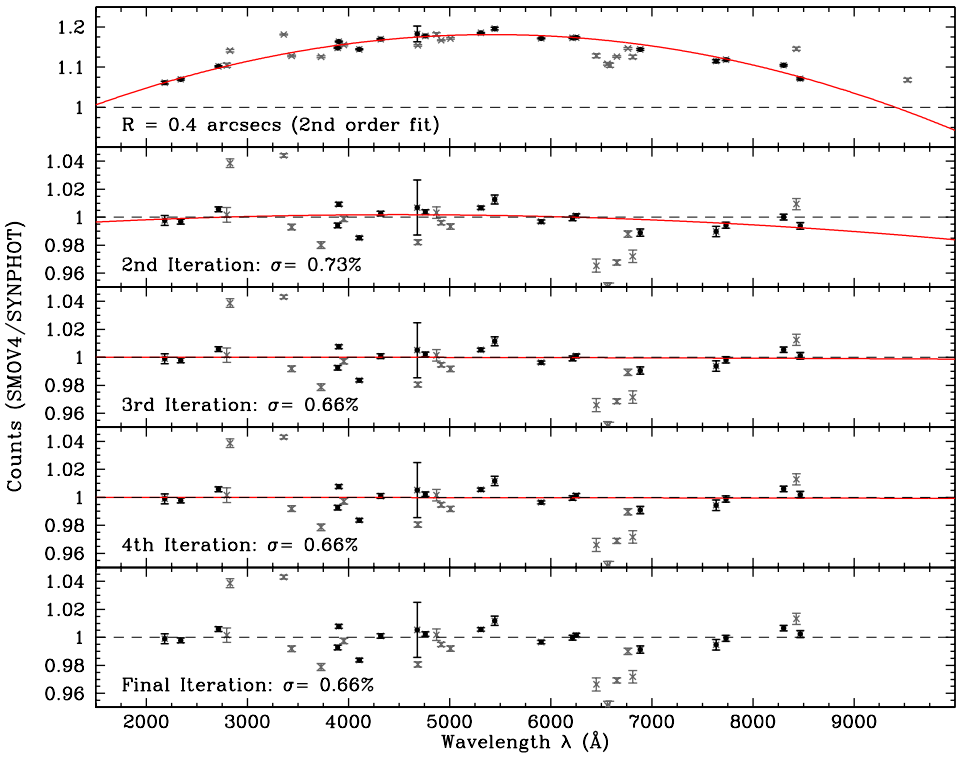

Fig. 6.— *The ratio of our measured on-orbit counts of GD 153 are compared to SYNPHOT predictions, and a 2nd order polynomial is fit to the ratios for the medium and wide band filters (red curve) in the top panel. In each successive panel, we illustrate the resulting comparison between our measured counts and a recalculation of SYNPHOT synthetic photometry with the previous correction factor, which then factors in the integral of the actual bandpass with the (new) full throughput. The new correction is multiplied by the old correction at each step of the iteration, and the measured standard deviation is shown to no longer improve by the 4th iteration. We note that the quoted 0.66% dispersion represents the measurement in all medium and wide band filters, with the exception of F336W which suffers from a poor flat field correction as discussed in Section 7.1.*

correction factor.

To begin this process, we fit a simple low order (2nd) polynomial to the ratios shown in Figure 5. We use all of the medium and wide band filters for this calculation, except for F336W which suffers from a poor (ground) flat field, as discussed earlier. This polynomial is illustrated in the top panel of Figure 6. The polynomial defines the first correction factor that we fold into SYNPHOT. We then recalculate synthetic photometry in each of these filters using SYNPHOT, and compare these to the actual measured photometry. The ratio of these counts is shown in the second panel of Figure 6, and clearly indicates that, even with just the initial correction, the new predicted and measured counts agree with one another remarkably well. The standard deviation

of the medium and wide band filters from this 2nd iteration is measured to be 0.73%. A new 2nd order polynomial is now fitted to these new ratios, multiplied by the first correction, and fed into SYNPHOT to generate another iteration of synthetic photometry. This procedure is repeated several times until the measured dispersion among the ratios ceases to improve, thus defining the final correction file. The final standard deviation, shown in the bottom panel of Figure 6 is 0.66%.

Figure 6 shows that the SYNPHOT predictions for most of the other filters not used in the comparison, such as narrow bands, agree to within a few percent of the actual measured counts. Given the extrapolation of the smooth curve to wavelengths $\lambda \gtrsim 8500$ Å (our reddest medium band filter), the predicted flux at ∼9500 Å will be several percent lower than our actual measurements in the narrow band F953N filter. However, our approach is consistent in using only medium and wide band filters, and other bluer narrow band filters also disagree with the trusted measurements by a few percent. The F953N filter is also affected by fringing and therefore the throughput is more uncertain. Finally, in comparing our results to ACS/WFC, we note De Marchi et al. (2004) were able to reproduce the observed count rates with synthetic photometry to within 0.5% in their broadband filters. However, their approach differed from ours in the sense that they clipped 25% of their wide band measurements (e.g., F475W and F606W) as these filters showed larger discrepancies, whereas we have retained all medium and wide band filters.

In Figure 7, we illustrate the ratio of the final SYNPHOT correction from the iterative method described above to the initial polynomial fit in the top panel. Over the bulk of our wavelength range, the iterative approach makes a small (<0.3%) difference in the final correction file, although at our longest wavelengths the correction approaches 1%.

7.3 The UVIS2 CCD

The SMOV4 GD 153 observations were all executed on the UVIS1 CCD on WFC3 (see Kalirai et al. 2009b for an outline of the respective SMOV4 and Cycle 17 calibration plans and goals). The behavior of the two CCDs, as measured during TV3, is qualitatively similar as a function of wavelength, and therefore we expect the same enhancement in efficiency measured here to also apply to the UVIS2 CCD. To confirm this, we have performed a similar analysis to that described in section 7.1 above on the bright white dwarf standard GRW+70d5824, which was observed in the SMOV4 UVIS Contamination Monitor Program (CAL11426 – Baggett et al. 2009). As summarized in Table 2, the observations of this star included a two point dither pattern with the 512 × 512 pixel subarray, on both CCDs (subarrays UVIS1-C512A-SUB and UVIS2-C512C-SUB). Sixteen filters were observed over multiple visits, each separated by roughly one week. As for our primary observations of GD 153, the S/N was $\gtrsim$100 in each of the individual exposures.

Baggett et al. (2009) present an analysis of the relative photometry of GRW+70d5824 over several visits, and demonstrate photometric stability in the output counts to <2%. For the present analysis, we utilize the observations taken after mid-July, where the position of the star was offset to avoid a bad column. The measured counts of the standard star are averaged over both dither

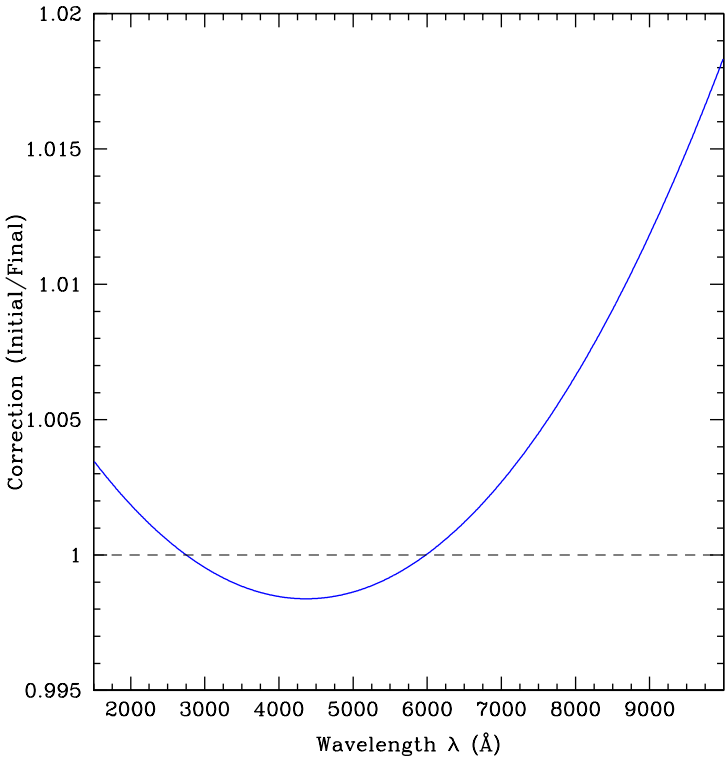

Fig. 7.— *The ratio of the initial SYNPHOT correction based on the iterative approach discussed in Section 7.2 to the final polynomial. The multiple iterations result in a negligible difference of <0.3% over most of the wavelength range, however, the correction improves by a larger amount at redder wavelengths. With the final correction, the measured dispersion in the counts vs SYNPHOT predictions, for all medium and wide band filters (except F336W – see Section 7.1), is 0.66% (see Figure 6, bottom panel).*

positions in Visits 31, 41, and 51 (separated by two weeks), and compared to SYNPHOT estimates for each CCD. The photometry was performed in the same apertures as for our GD 153 data, with the comparison to SYNPHOT being made at $R = 0.4$ arcseconds.

We highlight the results of this comparison in Figure 8 for both UVIS1 and UVIS2. The darker points represent the medium and wide band filters, and the grey points are the narrow and extra-wide filters. Given the known flat field errors from the bowtie, the F336W point has been plotted separately with a larger circle (note, the bowtie also effects the corner on the UVIS2 CCD where this star was observed). Assuming the correction factor from the GD 153 UVIS1 analysis, the GRW+70d5824 photometry is found to be consistent with SYNPHOT to $\sim$3 – 4% in all filters for UVIS1 and $\sim$2% for UVIS2. The measured standard deviation in the medium and wide band filters is 1.9% for UVIS1 and 1.6% for UVIS2. The UVIS1 counts have again been scaled downward by 3% to account for the pixel area map correction discussed earlier, whereas the UVIS2 pixel area map indicates the pixels have approximately the same area as those at the center of the mosaic,

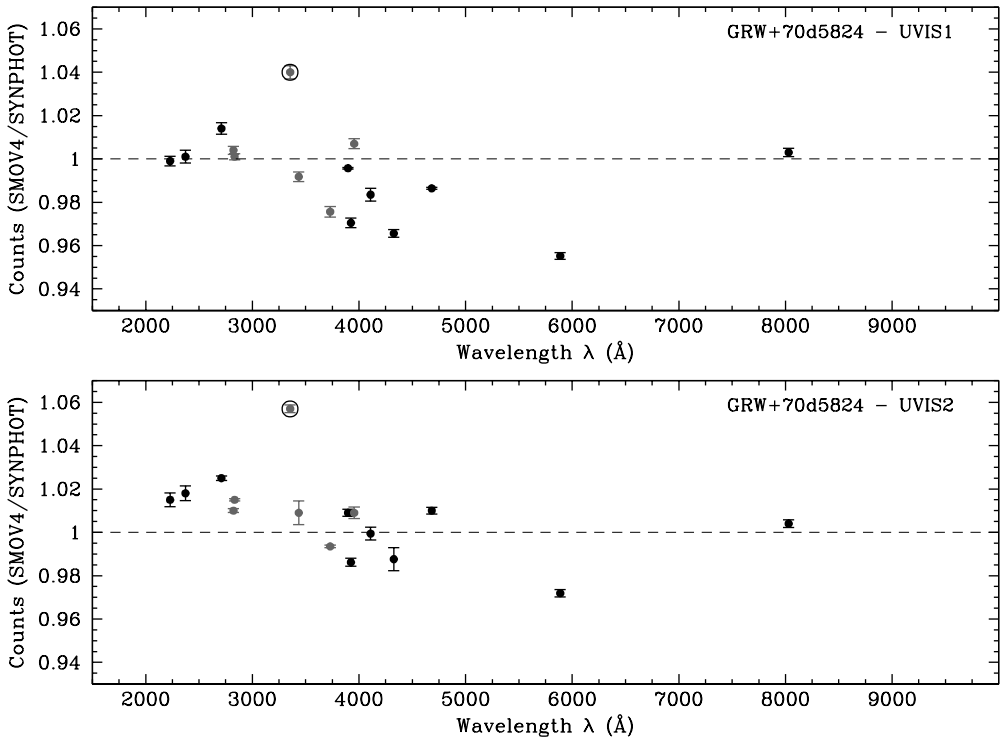

Fig. 8.— *The measured counts of the hot white dwarf GRW+70d5824, observed in the UVIS Contamination Monitor SMOV4 Program (CAL11426 – Baggett et al. 2009), are compared to SYNPHOT estimates after applying the correction based on our on-orbit measurements of GD 153. The solid points illustrate the ratio of measured counts to new SYNPHOT predictions for the medium and wide band filters, and the grey points represent the narrow band filters. The encircled point is F336W, which suffers from a poor flat field due to the bowtie. First, the general agreement between the top and bottom panels indicate that the same correction factor that we measured on UVIS1 can be applied to UVIS2 (and has been). Second, the standard deviation in the absolute agreement between the GRW+70d5824 measurements and the new SYNPHOT estimates is 1.9% for UVIS1 and 1.6% for UVIS2, in the medium and wide band filters. There is mild evidence for a slope in the wavelength dependence in both CCDs suggesting the possibility of a small error in the absolute flux calibration of this (secondary) HST standard.*

and therefore no correction has been applied. This analysis indicates that the same SYNPHOT correction factor calculated for UVIS1 can be applied to UVIS2. However, a detailed look at these two comparisons suggests the possible existence of a shallow trend in the ratio of measured to predicted counts for this star. The measured flux at bluer wavelengths appears to be higher than the predictions, with the overall trend showing a lower ratio at longer wavelengths up to F606W where the discrepancy is ∼4%. At F814W, the ratios agree nicely with the results calculated from GD 153. This may suggest a small error in the absolute flux calibration of GRW+70d5824, which

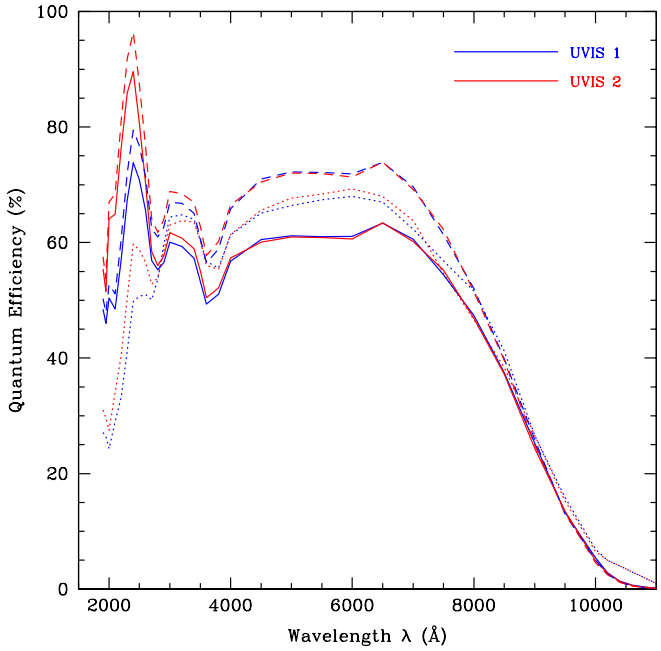

Fig. 9.— *The QE of the UVIS1 and UVIS2 detectors is shown, as measured at the DCL (dotted) and calibrated on the ground during TV3 tests (solid). The WFC3 detectors clearly have excellent sensitivity extending down to 200 nm. As discussed in Sections 7.1 and 7.2, it is not clear what fraction of the enhancement in counts seen on orbit can be attributed to the QE, as the total system throughput includes HST components, other instrument components, and filter transmission functions. Some fraction of the gain likely belongs in one or more of these other throughput tables, and therefore we have not adjusted the actual QE in SYNPHOT. Rather, the gain in throughput has been folded into the total throughput as an additional correction. The dashed lines illustrate what the QE would look like if we attributed 100% of the flight correction as a QE enhancement (as has been done for previous HST instruments).*

is a secondary HST standard not as well calibrated as GD 153. An analysis of this is underway and will be reported in a future ISR.

The detector QE of UVIS1 and UVIS2 is illustrated in Figure 9 (e.g., the number of electrons yielded per incident photon). The dotted curves illustrate the measured QE of the flight detectors as measured at the DCL at the Goddard Space Flight Center. The solid curves represent the current QE that is used in SYNPHOT for WFC3, which includes a ∼10% downward revision based on the latest ground tests in TV3 (Brown 2008). The dashed curves illustrate what the new detector QE would look like if we attributed 100% of the measured on-orbit correction from this analysis as a QE change. The total system throughput is a product of many components, and therefore some fraction of this flight correction likely belongs in a different component (e.g., the HST OTA). For

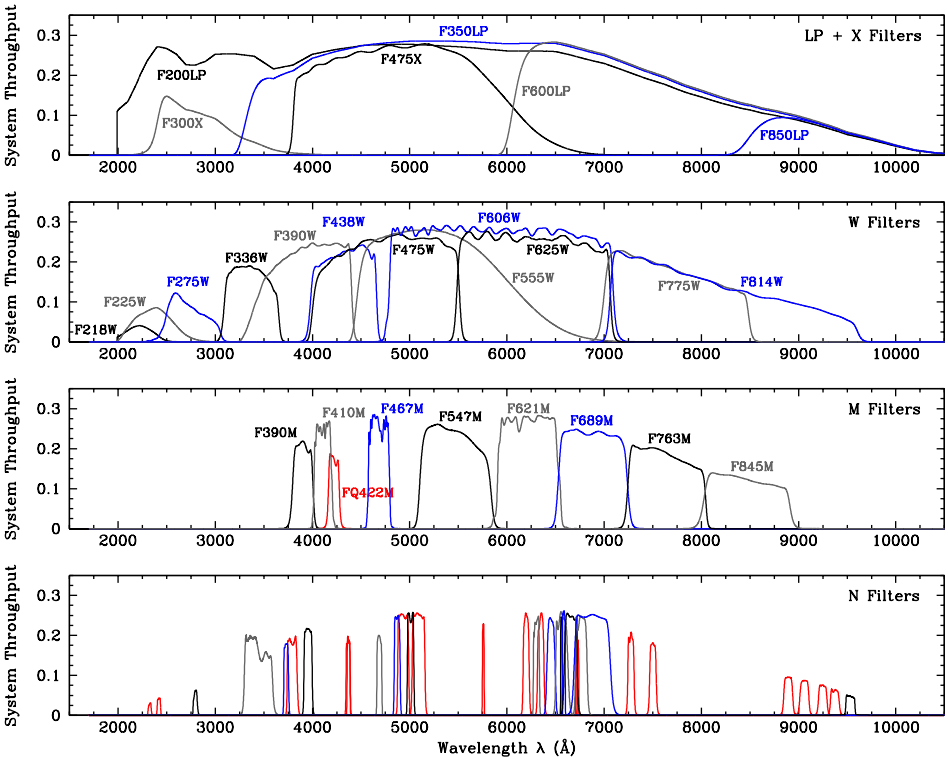

Fig. 10.— *The total system throughput through each of the WFC3 filters, including those that were not observed as a part of this program. The throughput accounts for all telescope and instrument components, as well as the correction factor derived from the first on-orbit observations in this ISR. The narrow band filters are not labelled for clarity. Further information on all of these filters is available in the IHB.*

the present calibration of the total system throughput, we have not adjusted the detector QE and rather folded the efficiency gain into a separate correction factor. The overall system throughput in each of our filters is summarized in Figure 10.

8. Photometric Zero Points

The photometric zero point of an instrument/filter combination is a convenient way to characterize the overall sensitivity. By most definitions, the zero point represents the magnitude of a star-like object that produces one count per second within a given aperture (see Maiz Apellaniz 2007). For the present work, the zero points depend on the absolute flux calibration of HST white dwarf spectra, and therefore will change whenever that calibration is improved. For WFPC2, Holtzman et al. (1995) measured photometric zero points in an intermediate-sized aperture of $R = 0.5$ arcseconds to alleviate uncertainties in the sky background for measurements made at larger apertures. These can include mapping the extended PSF wings, the digitized effects of the A/D converters, and CTE problems. Such an aperture is more convenient for typical point

source photometry, however it can not be used directly for surface photometry and will require a large correction. For ACS, Sirianni et al. (2005) use a much larger standard aperture of $R = 5.5$ arcseconds. Such an aperture is impractical for most point source photometry measurements, especially in crowded fields. However, Sirianni et al. (2005) point out that the ACS correction from a small to a large aperture varies strongly from filter to filter and the "infinite" aperture approach is the traditional SYNPHOT default and therefore a better conversion between point sources and extended sources will be enabled by this convention. Clearly, both approaches have advantages and, therefore, for WFC3, we compute zero points both for an infinite aperture and for $R = 0.4$ arcseconds. The former can also be scaled to the zero point in any aperture based on the enclosed energy fractions provided in Table 3.

Although the observed magnitude in any WFC3 filter is sufficient to define the camera's own photometric system (e.g., WFC3MAG = -2.5log(count rate [e$^-$ s^{-1}]), it is convenient to convert the measured brightnesses into a common photometric system. Such systems have been in place since the time of Hipparchus and very slowly evolved over time. Today, the most popular systems in use are the VEGAMAG, STMAG, and ABMAG, and so we define photometric zero points in each of these systems. These zero points, summarized in Tables 4 and 5, represent additive constants to translate the observed WFC3MAG measurements into the chosen system (e.g., STMAG = -2.5log(count rate [e$^-$ s^{-1}]) + ZP$_{STMAG}$), and should not be confused with the internal zero points of the system (see below).

Briefly, we summarize the definitions of the three photometric systems and refer readers interested in more details, including definitions and conversions between systems, to the nice discussion in Sirianni et al. (2005). The VEGAMAG system is defined such that the bright AOV star α-Lyrae (i.e., Vega) has a magnitude of 0 at all wavelengths. The system was/is convenient as Vega is a bright star that can be easily observed in the northern hemisphere, and contains a smooth spectrum with few features. The VEGAMAG system is the default SYNPHOT magnitude system, and the magnitude of a star with flux f in this system is simply $-2.5\log(f/f_{\rm Vega})$, where $f_{\rm Vega}$ is the calibrated spectrum of Vega in SYNPHOT. The STMAG and ABMAG systems are different in that they define an equivalent flux density for a source of predefined shape that would produce the observed count rate. In the STMAG system, the flux density is expressed per unit wavelength, and, in the ABMAG system, the flux density is express per unit frequency. The reference spectra are flat as a function of wavelength and frequency in each respective case. The definitions of the systems are STMAG = $-2.5\log(f_\lambda) - 21.10$ (where f_λ is expressed in erg cm^{-2} s^{-1} Å^{-1}) and ABMAG = $-2.5\log(f_\nu) - 48.60$ (where f_ν is expressed in erg cm^{-2} s^{-1} Hz^{-1}). The offsets in these equations, e.g., -21.10 and -48.60, are also frequently referred to as zero points. However, these are a part of the definition of the photometric system. For example, in the STMAG system, the zero point of -21.10 is set so an object with this brightness will have a flux density of 1 erg cm^{-2} s^{-1} Å^{-1}. The zero points that we list in Tables 4 and 5 account for this internal offset and for the flux density that produces a response of one count per second in the respective WFC3 filters. Therefore, the magnitude of a star in the given photometric system can be simply calculated by measuring its

count rate and adding the zero point from the table.

Finally, we discovered an error in the calculation of SYNPHOT photometric keywords during our analysis. The published zero point tables on the STScI webpage for ACS include the PHOTBW column, which represents the rms bandwidth of the filter, convolved with the total system throughput. The calculation in SYNPHOT that defines this parameter computes the integral of the bandpass over a very wide wavelength range. Although the throughput over 99% of the range (e.g., in the narrow band filters) is of order $1 \times 10^{-}7$ (or less), this extra data skews the measured bandwidth given roundoff errors and imprecision. Unfortunately, this parameter is also embedded into the header of processed HST data, both for ACS and WFC3. The correct value can be easily calculated by limiting the integral over the region of sensitivity of the filter in SYNPHOT.

Table 4: Photometric Zero Points for WFC3/UVIS1, Calculated for an Infinite Aperture

Filter	PHOTFLAM[a]	STMAG	ABMAG	VEGAMAG
F218W	1.462×10^{-17}	20.99	22.94	21.25
F225W	4.598×10^{-18}	22.24	24.06	22.40
F275W	3.260×10^{-18}	22.62	24.14	22.65
F280N	5.708×10^{-17}	19.51	20.94	19.51
F300X	1.472×10^{-18}	23.48	24.92	23.50
F336W	1.342×10^{-18}	23.58	24.64	23.46
F343N	2.542×10^{-18}	22.89	23.90	22.75
F350LP	5.327×10^{-20}	27.08	26.94	26.78
F373N	1.324×10^{-17}	21.10	21.93	21.04
F390M	2.520×10^{-18}	22.90	23.64	23.54
F390W	5.045×10^{-19}	24.64	25.37	25.15
F395N	5.993×10^{-18}	21.96	22.66	22.68
F410M	2.310×10^{-18}	22.99	23.61	23.77
F438W	6.807×10^{-19}	24.32	24.83	24.98
F467M	1.636×10^{-18}	23.37	23.71	23.86
F469N	9.416×10^{-18}	21.47	21.80	21.96
F475W	2.533×10^{-19}	25.39	25.69	25.79
F475X	1.539×10^{-19}	25.93	26.15	26.21
F487N	5.975×10^{-18}	21.96	22.21	22.03
F502N	5.204×10^{-18}	22.11	22.30	22.39
F547M	4.747×10^{-19}	24.71	24.72	24.72
F555W	1.876×10^{-19}	25.72	25.78	25.81
F600LP	8.959×10^{-20}	26.52	25.85	25.53
F606W	1.165×10^{-19}	26.23	26.08	25.99
F621M	4.097×10^{-19}	24.87	24.59	24.45
F625W	1.738×10^{-19}	25.80	25.52	25.37
F645N	3.309×10^{-18}	22.60	22.24	22.05
F656N	1.538×10^{-17}	20.93	20.54	19.92
F658N	9.287×10^{-18}	21.48	21.08	20.72
F665N	1.969×10^{-18}	23.16	22.74	22.50
F673N	2.217×10^{-18}	23.04	22.58	22.34
F689M	3.756×10^{-19}	24.96	24.47	24.19
F763M	3.921×10^{-19}	24.92	24.20	23.82
F775W	2.145×10^{-19}	25.57	24.85	24.47
F814W	1.559×10^{-19}	25.92	25.09	24.67
F845M	4.730×10^{-19}	24.71	23.77	23.27
F953N	9.385×10^{-18}	21.47	20.27	19.65

[a]PHOTFLAM is the inverse sensitivity; the flux density of a star that produces a response of one count per second in this band pass, measured in ergs cm^{-2} s^{-1} $Å^{-1}$.

Table 5: Photometric Zero Points for WFC3/UVIS1, Calculated for $R = 0.4$ arcseconds

Filter	STMAG	ABMAG	VEGAMAG
F218W	20.82	22.77	21.08
F225W	22.08	23.90	22.24
F275W	22.48	24.00	22.51
F280N	19.37	20.80	19.37
F300X	23.34	24.78	23.36
F336W	23.46	24.52	23.34
F343N	22.77	23.78	22.63
F350LP	26.98	26.84	26.68
F373N	20.99	21.82	20.93
F390M	22.79	23.53	23.43
F390W	24.53	25.26	25.04
F395N	21.85	22.55	22.57
F410M	22.89	23.51	23.67
F438W	24.22	24.73	24.88
F467M	23.27	23.61	23.76
F469N	21.37	21.70	21.86
F475W	25.29	25.59	25.69
F475X	25.83	26.05	26.11
F487N	21.86	22.11	21.93
F502N	22.01	22.20	22.29
F547M	24.61	24.62	24.62
F555W	25.62	25.68	25.71
F600LP	26.42	25.75	25.43
F606W	26.13	25.98	25.89
F621M	24.77	24.49	24.35
F625W	25.70	25.42	25.27
F645N	22.50	22.14	21.95
F656N	20.83	20.44	19.82
F658N	21.38	20.98	20.62
F665N	23.06	22.64	22.40
F673N	22.94	22.48	22.24
F689M	24.86	24.37	24.09
F763M	24.82	24.10	23.72
F775W	25.47	24.75	24.37
F814W	25.82	24.99	24.57
F845M	24.61	23.67	23.17
F953N	21.36	20.16	19.54

9. Summary, Implications, and a Look Forward to Cycle 17

The first on-orbit observations of GD 153, an HST spectrophotometric standard, suggest that the absolute throughput of WFC3/UVIS is ∼10 – 20% higher than measured in the latest TV3 campaign. We have characterized this efficiency gain with a smooth polynomial and factored it into the existing SYNPHOT throughput tables as an additional correction. In practice, this new throughput file, which is called wfc3_uvis_cor_003_syn.fits, replaces a previous file that was held flat with entries of "1.0" throughout. Relative to the previous SYNPHOT counts from TV3, the new counts can be estimated by multiplying the old values by $f = 0.838 + 1.279(\lambda) - 1.191*(\lambda)^2$, where λ is the wavelength in micrometers. These changes have been reflected in the WFC3 pipeline and new photometric keywords in the headers of processed data will provide the updated results. The new files can be downloaded from the STScI WFC3 reference files webpage.[5]

WFC3/UVIS has a higher throughput than any HST instrument over the wavelength range extending from its blue cutoff (at 2000 Å) to ∼4000 Å. Beyond this limit, the choice of which HST instrument is best suited for users depends on the details of the science requirements. Although the absolute throughput of ACS is higher at optical wavelengths, the highest WFC3 efficiency gains in our on-orbit observations also occur at 4000 – 7000 Å, and therefore the gap between the two instruments has been closed significantly. Specifically, some of the primary science observations with HST require several orbits where signal is coadded over multiple exposures. Relative to ACS/WFC, WFC3 has smaller pixels by 20%, a lower read noise by ∼50%, negligible CTE corrections, and a much lower dark current. Combined with our new efficiency measurements, the ability to better sample the PSF and naturally beat down the noise through multiple exposures can make WFC3 the preferred instrument for even broadband F606W and F814W observations of faint sources. For example, the two instruments will both reach a limiting ABMAG of 27.9 (29.2) for a S/N = 10 point source detection in 1 hour (10 hours) in the F606W filter. The choice between the two instruments will require careful predictions from the respective ETCs, factoring in the detailed observational setup. Of course, WFC3 contains many more filters over its complete wavelength range than ACS/WFC, yet ACS offers a 50% larger field of view, both considerations being potentially important for users.

As summarized in Kalirai et al. (2009b), the SMOV4 observations to characterize WFC3's sensitivity are quite limited. A large Cycle 17 calibration effort measures the photometric zero points in all filters, on both CCDs of the camera (CAL11903 – PI Kalirai). Comparisons will be drawn with other bright primary HST spectrophotometric standards such as G191-B2B and GD 71. We will also obtain observations of cooler spectrophotometric standards, such as the solar analog P330E, and obtain star cluster observations to characterize color terms and photometric transformations between WFC3 filters and other systems.

[5] `http://www.stsci.edu/hst/observatory/cdbs/SIfileInfo/WFC3/reftablequeryindex`

Acknowledgements

We thank the entire WFC3 team for their many years of dedicated effort in producing and calibrating the instrument.

References

Baggett, S., et al. 2009, WFC3 ISR 2009 — (CAL11426), in preparation
Bergeron, P., Saffer, R. A., & Liebert, J. 1992, ApJ, 394, 228
Bohlin, R. C., Colina, L., & Finley, D. S. 1995, AJ, 110, 1316
Bohlin, R. C. 1996, AJ, 111, 1743
Bohlin, R. C. 2000, AJ, 120, 437
Bohlin, R. C., Dickinson, M. E., & Calzetti, D. 2001, AJ, 122, 2118
Bohlin, R. C. 2007, ACS ISR 2007-06, "Photometric Calibration of the ACS CCD Cameras"
Brown, T. M., & Reid, I. N. 2005, WFC3 ISR 2005-02, "Results of WFC3 Thermal Vacuum Testing – UVIS Channel Throughput"
Brown, T. M. 2007, WFC3 ISR 2007-07, "WFC3 System Throughput on the UVIS Build 2 Detector"
Brown, T. M. 2008, WFC3 ISR 2008-48, "WFC3 TV3 Testing: System Throughput on the UVIS Build 1' Detector"
Brown, T. M., Hartig, G., & Baggett, S. 2008, WFC3 ISR 2008-10, "WFC3 TV3 Testing: UVIS Window Contamination"
De Marchi, G. 2004, ACS ISR 2004-08, "Detector Quantum Efficiency and Photometric Zero Points of the ACS"
Finley, D. S., Koester, D., & Basri, G. 1997, ApJ, 488, 375
Hartig, G., & Dressel, L. 2009, WFC3 ISR 2009 — (CAL11438), in preparation
Holtzman, J. A., Burrows, C. J., Casertano, S., Hester, J. J., Trauger, J. T., Watson, A. M., & Worthey, G. 1995, PASP, 107, 1065
Kalirai, J., et al. 2009a, WFC3 ISR 2009-30 (CAL11451), in preparation
Kalirai, J., et al. 2009b, WFC3 ISR 2009-05, "The Photometric Calibration of WFC3: SMOV and Cycle 17 Observing Plan"
Kalirai, J., et al. 2009c, WFC3 ISR 2009 —, in preparation (Cosmic Ray Rejection)
Kalirai, J., et al. 2009d, WFC3 ISR 2009 —, in preparation (Pixel Area Maps)
Khozurina-Platais, V. et al. 2009, WFC3 ISR 2009 — (CAL11444), in preparation
Maiz Apellaniz, J. 2007, ASP, 364, 227
Sabbi, E., Dulude, M., Martel, A. R., Baggett, S., & Bushouse, H. 2008, WFC3 ISR 2008-46, "WFC3 UVIS Ground P-flats"
Sabbi, E., et al. 2009, WFC3 ISR 2009-19 (CAL11452), in preparation
Sirianni, M., de Marchi, G., Gilliland, R. L., Bohlin, R. C., Pavlovsky, C., & Mack, J., 2002, HST Calibration Workshop, 31

Sirianni, M., et al. 2005, PASP, 117, 1049
Stetson, P. B. 1987, PASP, 99, 191
Stetson, P. B. 1994, PASP, 106, 250
van Dokkum, P. G. 2001, PASP, 113, 1420